

Synchronous Microlens Transfer-Printing Packaging for High-Efficiency Micro-LED Arrays

Tsung-Hao Su,* Ming-Yu Lou, Wen-De Xie, Ting-Hao Liu, Sun-Zen Chen, and Jwo-Huei Jou



Cite This: <https://doi.org/10.1021/acsaom.5c00641>



Read Online

ACCESS |

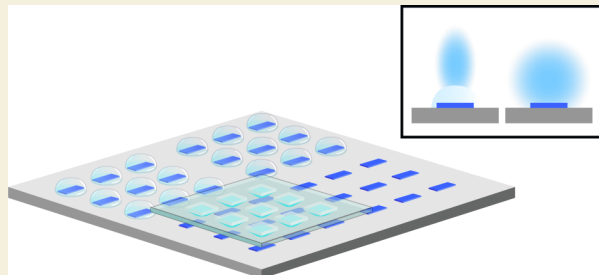
Metrics & More

Article Recommendations

Supporting Information

ABSTRACT: Microlight-emitting diodes (micro-LEDs) exhibit high brightness, low power consumption, and fast response, making them highly promising for next-generation displays and optical communication. However, conventional planar encapsulation limits the light extraction efficiency (LEE) and emission directionality, constraining overall luminous performance. Here, we propose a mask-free synchronous-alignment microlens transfer-printing technique capable of packaging thousands to tens of thousands of pixels simultaneously. At a drive current density of 100 A cm^{-2} , the forward luminance increases from 6.5 to 9.6 Mcd m^{-2} (+48%) and the external quantum efficiency (EQE) increases from 19% to 29% (+53%) compared to planar packaging. To reach a target luminance of 10 Mcd m^{-2} , the required drive current density is reduced by ~45%. Angular measurements show the emission range expanding from 60° – 120° to about 30° – 150° , with significantly enhanced on-axis output. Overall, this technique combines high alignment precision and yield with significant LEE/EQE gains, tunable directionality, and lower drive currents, making it viable for mass-produced applications such as visible light communication (VLC), copackaged optics (CPO), and high-density microdisplays.

KEYWORDS: *micro-LED, microlens, light extraction efficiency, external quantum efficiency, visible light communication, copackaged optics*



1. INTRODUCTION

Wearable devices, AR/VR (Augmented Reality/Virtual Reality) systems, and high-resolution microdisplays are rapidly evolving, finding applications in near-eye displays, smart sensing, and optical communication modules. Micro-LED arrays have also been explored as compact microillumination platforms, where optical efficiency and emission control are critical to system-level performance.¹ In these contexts, microlight-emitting diodes (Micro-LEDs) are widely recognized as a key enabling technology.^{2,3} Owing to their self-emissive nature, high brightness, high contrast, and long-term stability, micro-LEDs can overcome the performance limitations of LCDs and OLEDs in certain applications, enabling highly integrated and high-performance optoelectronic systems.^{2,3} Moreover, micro-LEDs support nanosecond-scale modulation and excellent optoelectronic conversion efficiency, which has led to their adoption in high-speed, highly integrated photonic architectures such as visible light communications (VLC), optical wireless communications (OWC), and copackaged optics (CPO).^{4–6} Recent micro-LED-enabled retinal projection architectures for AR near-eye displays further highlight the growing demand for compact, high-brightness emissive sources with well-controlled output in next-generation optical systems.⁷ For optical wireless links, a recent massive GaN micro-LED array transmitter has been used to extend underwater wireless optical communication distance while

maintaining high data rates, illustrating the strong system-level dependence on forward optical power and angular control.⁸

However, practical deployment of micro-LEDs faces significant challenges. The most critical limitation arises from the miniaturized LED geometry: when the device size shrinks to the micrometer scale, total internal reflection and waveguiding at the semiconductor/air interface become severe, causing the light extraction efficiency (LEE) to drop markedly.^{9,10} This reduction in LEE suppresses emission intensity and communication range. Simultaneously, micro-LED system integration must address packaging requirements for chip protection, thermal management, and optical coupling, imposing stringent demands on fabrication precision and alignment tolerance. In particular, for high-speed optical communication modules, insufficient control over emission directionality and intensity uniformity directly affects system sensitivity and channel stability, becoming a major bottleneck for practical implementation.^{11,12}

Received: December 23, 2025

Revised: January 28, 2026

Accepted: January 28, 2026

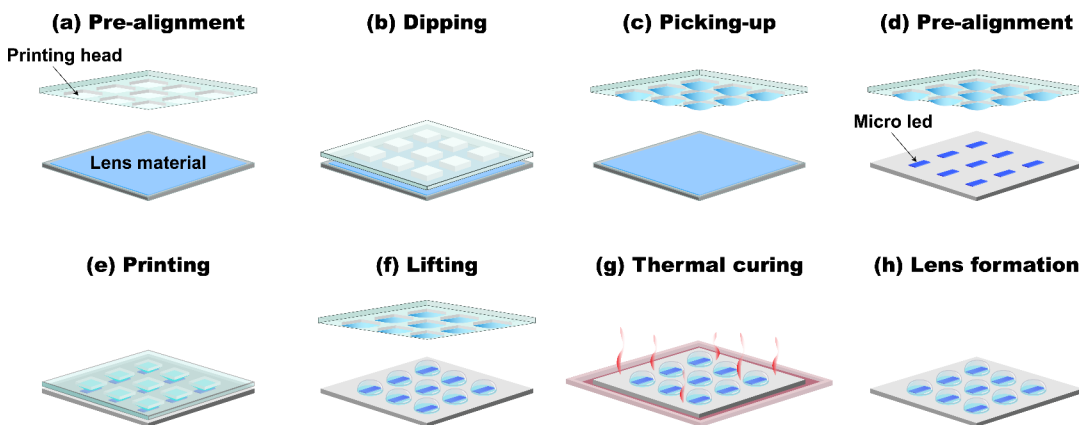


Figure 1. Schematic of transfer-printed microlens encapsulation. (a) Prealignment and inking, (b) pickup of equal-volume droplets, (c–d) CCD-assisted alignment to Micro-LED pixels, (e) transfer, (f) lift-off preserving hemispherical profiles, and (g–h) thermal curing to yield a registered microlens array.

Given these challenges, packaging technology plays a critical role in achieving high-efficiency, high-integration micro-LED systems. An ideal package must not only protect the chip but also shape the optical field, dissipate heat, and provide accurate mechanical alignment. Conventional approaches often use simple planar encapsulation or direct bonding, which at the microscale can introduce severe optical scattering and internal reflection losses. These losses lead to unstable emission directionality and significantly reduced LEE,^{13,14} thereby limiting the overall optical communication efficiency and device stability.

To overcome these limitations, microlens encapsulation has been increasingly applied to micro-LED structures. Early demonstrations of GaN micro-LED arrays with monolithically integrated sapphire microlenses already indicated the potential of pixel-level micro-optics for enhancing light extraction and shaping emission.¹⁵ Forming spherical or aspherical microlenses on the emitting surface can redirect scattered or escaping light back into the forward emission cone, not only enhancing forward output intensity but also improving angular dependence and field uniformity.¹⁶ Such secondary optics are especially beneficial for optical communication modules requiring collimation and coupling (e.g., optical waveguides, VLC, fiber coupling). For example, Wu et al. demonstrated micro-LEDs with external microlenses and low-index protection layers, achieving ~45% higher forward intensity than bare LEDs.¹³ Wang et al. integrated microlenses and nanoscale features into pixel packages, compressing the emission half-width (fwhm) from 138° to 72° and raising LEE to 18.4%.¹⁷ They also noted that microlens geometry (height and curvature) has a decisive impact on beam direction and energy redistribution. Lately, a “mushroom-cap” encapsulated LED array integrating hemispherical micro-optics was reported to confine Lambertian emission into a narrow angular range and enhance the central intensity, underscoring the role of encapsulation morphology in beam shaping for compact near-eye/projection engines.¹⁸ In parallel, broadband beam-collimation metasurfaces have also been demonstrated for full-color micro-LED displays, achieving reduced divergence and increased on-axis intensity, further emphasizing that engineered secondary-optics geometry critically governs angular emission and system-level coupling.¹⁹ More recently, freeform microlens arrays have been designed with prescribed luminance distributions for micro-LED optical packaging,

further highlighting microlens geometry as a key design degree of freedom for angular control and brightness management.²⁰

However, these strategies typically rely on multilayer stack structures and photolithography, which limit alignment tolerance and are difficult to implement in mass-transfer processes.^{17,21,22} Meanwhile, common microlens fabrication techniques such as dispensing or inkjet printing, while automated and scalable, suffer at the microscale from droplet misplacement, material wettability variations, and shape variability. These issues cause spot misalignment and unstable emission, limiting their utility in high-speed optical communication modules.^{23,24}

To address these challenges, we propose a packaging strategy that combines mass transfer with synchronous microlens alignment. Using an elastomeric transfer head and high-precision vision guidance, we simultaneously transfer the micro-LED chips and form the microlenses in one step. This synchronized process achieves high alignment precision, simplifies the fabrication flow, and ensures high reproducibility. Because the microlens array registration is executed within the same CCD-referenced coordinate system as the micro-LED pixel array, the process avoids step-to-step overlay accumulation that commonly arises when lens formation and lens-to-pixel alignment are performed as separate process modules. The microlens height can be adjusted according to application needs to further optimize emission directionality and angular distribution. Consequently, this approach realizes a packaging integration that delivers both luminance gain and expanded angular coverage.

2. EXPERIMENTAL DETAILS

We developed a high-throughput, large-area microlens transfer-printing encapsulation process for micro-LED arrays. The workflow comprises four steps: (1) spin-coating the lens material, (2) inking the elastomeric micropillar stamp, (3) precision alignment/transfer onto the micro-LED array, and (4) thermal curing to form hemispherical microlenses. The process is compatible with existing mass-transfer tools without additional equipment development, thereby reducing process complexity and capital cost. A single print covers thousands to tens of thousands of pixels with high overlay yield, highlighting applicability to next-generation micro-LED displays and copackaged optics (CPO) modules.

The transfer system consists of a micropillar stamp, a high-resolution CCD imaging module, and a motorized XYZ stage. During inking, controlled Z-indentation contact – dwell – normal retraction

is used to load equal-volume droplets onto the pillar tips. During printing, CCD-assisted X/Y alignment registers each droplet to the micro-LED emission center, followed by Z-axis approach and normal separation. The overlay accuracy is approximately $\pm 1 \mu\text{m}$.

Achieving submicron overlay is currently limited by (i) vision metrology (camera sampling/optics and feature/centroid extraction), (ii) stage repeatability and environmental drift, and (iii) compliance-induced microdistortion or slip during stamp contact and retraction. Unlike dispensing/inkjet approaches where droplet landing and substrate wetting can introduce placement scatter prior to curing, our droplets are first metered on the micropillar stamp and then registered to the pixel emission centers by CCD before contact and transfer, thereby reducing placement variability at the microscale. Contact depth, dwell time, and peel/retraction speed are executed under fixed recipes to ensure run-to-run reproducibility.

A silicone-based polymer (refractive index ≈ 1.6 in the visible) was used as the microlens material. The detailed sequence (Figure 1a–h) is as follows: a $\approx 30 \mu\text{m}$ film was formed on a temporary carrier by spin-coating at 3000 rpm for 30 s; the micropillar stamp was brought into precise, controlled-depth contact with the film to ink monodisperse droplets (dwell on the order of hundreds of milliseconds, then vertical retraction); the inked stamp was moved to a region-selectively treated micro-LED array, prealigned by CCD and fine-tuned so that each droplet coincided with its target pixel center; Z-axis approach completed the transfer, followed by rapid normal lift-off to preserve the hemispherical droplet profile and positional accuracy; finally, thermal curing was performed at 120°C for ~ 30 min to form transparent hemispherical microlenses. After curing, each micro-LED was capped by a one-to-one, well-registered microlens. The synchronous transfer/encapsulation flow is highly reproducible, requires no photolithography, and avoids the micron-scale placement errors often seen in dispensing/inkjet approaches—facilitating adoption in high-speed optical communication and CPO systems. Microlens height (h) was tuned by a controlled dip (inking) condition and, when needed, by repeating the dip-and-cure sequence to incrementally increase the deposited polymer volume. Importantly, the lateral aperture (w) is primarily constrained by the microsphere-/stamp-defined footprint and thus remains essentially constant, allowing h (and equivalently h/w) to be adjusted as the main morphological tuning knob.

Overlay accuracy and 2D/3D surface profiles were measured using a Keyence VK-X3000 laser confocal microscope. Optical characterization employed a CAS-120 spectroradiometer (Instrument Systems, Germany) coupled to a 25 cm integrating sphere and a collimation tube, calibrated across the visible band, to obtain luminous flux (lm) and forward luminance (cd m^{-2}). Angular emission profiles were measured from 0 – 180° using an LEDGON 100 goniophotometer under constant-current drive. All electrical measurements were conducted at room temperature ($\sim 25^\circ\text{C}$) in ambient air using a Keithley 2400 source meter for constant/stepped-current operation with simultaneous electrical logging to ensure stability and reproducibility. ($\theta = 90^\circ$ corresponds to the surface normal).

The external quantum efficiency (EQE) was determined as the ratio of the emitted photon rate to the injected electron rate. The spectral radiant flux collected by the integrating sphere was measured using a calibrated spectroradiometer, yielding $\Phi_e(\lambda)$ (W nm^{-1}). The total photon emission rate was then obtained by converting radiant power into photon number via the photon energy $E_{ph} = hc/\lambda$, as shown in eq 1:

$$\Phi_{ph} = \int \frac{\Phi_e(\lambda)}{hc/\lambda} d\lambda = \int \frac{\Phi_e(\lambda) \cdot \lambda}{hc} d\lambda \quad (1)$$

where h is Planck's constant and c is the speed of light. The injected electron rate is given by I/e , where I is the drive current measured by a source meter (Keithley) and e is the elementary charge. Accordingly, the EQE is calculated using eq 2:

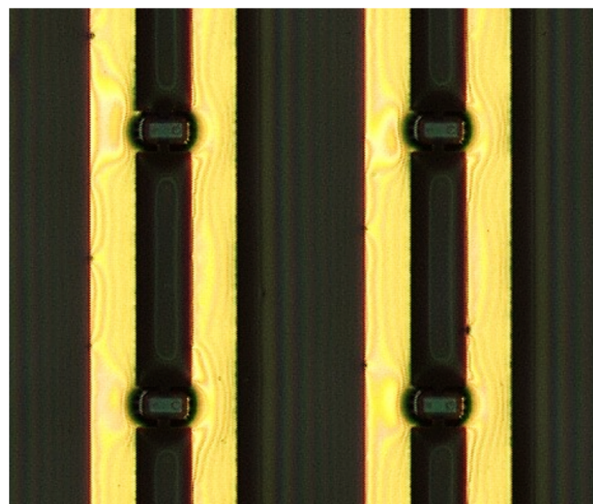
$$EQE = \frac{\Phi_{ph}}{I/e} \quad (2)$$

Luminance (cd m^{-2}) and luminous flux (lm) were also obtained from the calibrated spectroradiometer output under identical electrical driving conditions.

3. RESULTS AND DISCUSSION

Figure 2 presents laser-confocal micrographs of the Micro-LED array before and after microlens encapsulation. Following

(a)



(b)

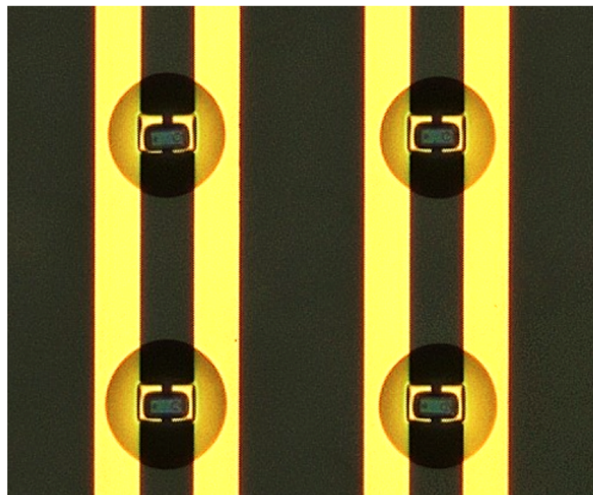


Figure 2. Laser-confocal images of the Micro-LED array before (a) and after (b) microlens encapsulation, showing uniform lens shape and accurate pixel-to-lens registration.

encapsulation, each pixel is capped by a transparent, dome-shaped microlens arranged in a well-registered grid. The lenses show uniform contour without voids or edge defects, and the pixel-to-lens registration is consistent with the measured overlay accuracy ($\approx \pm 1 \mu\text{m}$). These observations indicate that the synchronous transfer-printed process delivers high placement precision and shape repeatability on dense arrays, supporting stable optical performance for high-resolution, large-area modules.

Figure 3 shows 3D laser-confocal surface profiles. Prior to encapsulation, the LED mesa height on the substrate is $\approx 10 \mu\text{m}$. After encapsulation, each pixel forms a hemispherical microlens with a postcure height $h \approx 75 \mu\text{m}$ and smooth

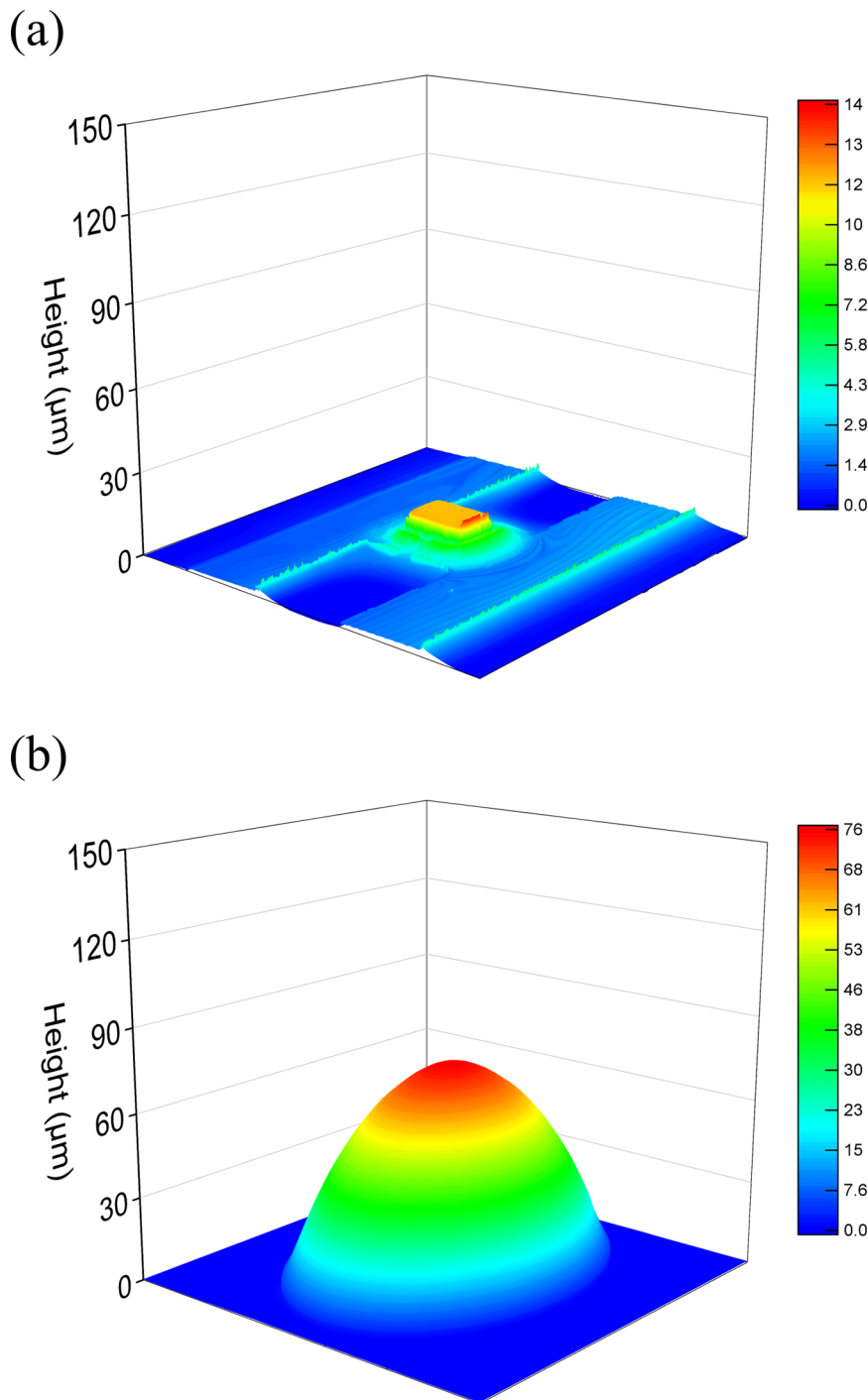


Figure 3. 3D laser-confocal profiles of a single pixel before (a, bare chip $\approx 10 \mu\text{m}$) and after (b, microlens $\approx 75 \mu\text{m}$) encapsulation, confirming the designed hemispherical geometry.

curvature. The curved refractive interface expands the effective escape cone and suppresses waveguiding/total-internal-reflection losses at the chip/air boundary, thereby increasing light-extraction efficiency (LEE) and strengthening near-normal emission. This 3D confocal topography provides direct morphology evidence of the cured polymer microlens. For transparent polymers, SEM imaging may require conductive coating and can be less straightforward for contrast; therefore, we use 3D laser confocal microscopy as a practical, nondestructive approach to obtain height-resolved profiles that directly quantify the lens curvature and height distribution,

enabling correlation between the dome-like geometry and the angular redistribution trends in Figure 7 and Table S3.

We compared the optoelectronic performance under different encapsulation conditions. Figure 4a,b shows that a conventional planar film deteriorates both forward luminance and EQE over the entire current-density range. At $J = 100 \text{ A cm}^{-2}$, the bare chip reaches 9.14 Mcd m^{-2} , whereas planar encapsulation reduces the forward luminance to 6.50 Mcd m^{-2} (-29%). In parallel, EQE decreases from 24.9% to 19.0% (-24%). The inset in Figure 4a replots the L-J relationship with a logarithmic current-density axis to highlight the low-

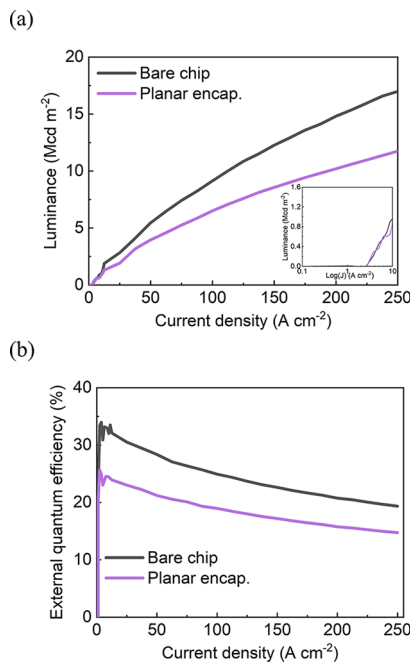


Figure 4. Impact of planar encapsulation on device performance: (a) forward luminance and (b) EQE of the bare chip and the planar-encapsulated device as a function of current density. Inset in (a): luminance plotted with a logarithmic current-density axis to highlight the low-current regime.

current regime, confirming that the planar film does not improve the low-injection output. This degradation is consistent with increased Fresnel losses and enhanced photon trapping caused by waveguiding and total internal reflection within the planar encapsulation layer, which collectively reduce the effective escape probability and thus the forward output.

In contrast, microlens encapsulation not only recovers but markedly enhances emission (Figure 5a,b). At the same drive condition ($J = 100 \text{ A cm}^{-2}$), the forward luminance increases from 6.50 Mcd m^{-2} (planar) to 9.60 Mcd m^{-2} (+48%), while the EQE improves from 19.0% to 29.0% (+53%). The hemispherical microlens functions as a refractive element that redirects rays that would otherwise be trapped or emitted laterally into more near-normal directions, thereby increasing forward output and improving the effective light-extraction efficiency. Mechanistically, the curved polymer/air interface increases the effective escape cone by refracting high-angle rays toward the surface normal, thereby reducing total internal reflection and lateral waveguiding that are pronounced in planar films. In addition, the lens geometry redistributes the angular power toward near-normal directions, increasing the measured forward luminance and improving coupling to free-space or downstream optics. Finally, because the target luminance can be reached at a substantially lower current density (Table 1), the practical operating point experiences reduced high-injection loss, which contributes to the observed EQE benefit under application-relevant conditions. From a processing standpoint, synchronous microlens transfer-printing requires no additional lithography steps and is compatible with existing mass-transfer hardware, providing a scalable route for array-level optical packaging with reduced process complexity. To quantify efficiency droop across different encapsulation conditions, we define droop (%) as $(\text{EQE}_{\text{peak}} - \text{EQE}@J)/\text{EQE}_{\text{peak}} \times 100\%$ and summarize the extracted values at $J =$

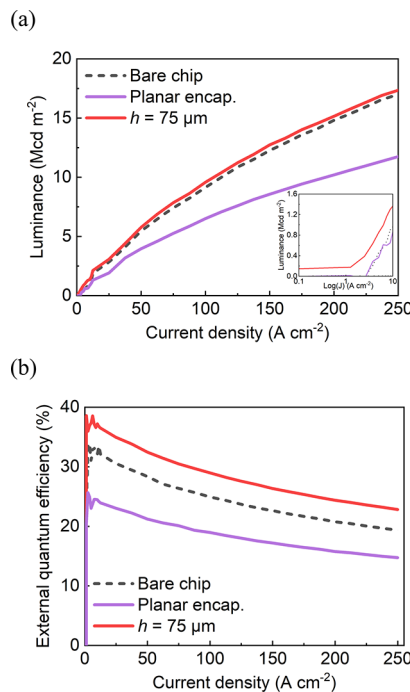


Figure 5. Performance enhancement enabled by hemispherical microlens encapsulation ($h = 75 \mu\text{m}$): (a) forward luminance and (b) EQE of bare, planar-encapsulated, and microlens-encapsulated devices as a function of current density. Inset in (a): luminance replotted with a logarithmic current-density axis to emphasize the low-current regime.

Table 1. Drive Current Density J (A cm^{-2}) Required to Achieve Luminances L of 1, 5, and 10 Mcd m^{-2} for Bare, Planar-Encapsulated, and Microlens-Encapsulated Devices^a

| Encapsulation conditions | Height (μm) | Current density (A cm^{-2}) | | |
|--------------------------|--------------------------|--|-----------------------|------------------------|
| | | 1 Mcd m^{-2} | 5 Mcd m^{-2} | 10 Mcd m^{-2} |
| Bare chip | — | 21 | 46 | 112 |
| Planar | — | 31 | 70 | 194 |
| Microlens | 75 | 18 | 43 | 106 |
| | 45 | 22 | 51 | 128 |
| | 25 | 28 | 58 | 139 |

^aNote: Microlens heights are measured after curing. “—” indicates not applicable.

100 and 250 A cm^{-2} , as well as at a matched luminance of 10 Mcd m^{-2} , in Table S1 (Supporting Information).

We further examined the impact of microlens height. Figure 6a,b compares devices with $h = 25, 45$, and $75 \mu\text{m}$. Because the aperture diameter w is constrained by the microsphere-/stamp-defined footprint (and is well controlled; see Figure S3 and Table S2), varying h via the dip-and-cure control effectively tunes the aspect ratio h/w (and the associated curvature). Therefore, the observed trends should be interpreted in terms of overall encapsulation morphology rather than height alone. Increasing h consistently boosts both luminance and EQE; for example, at $J = 100 \text{ A cm}^{-2}$ the forward luminance increases from 7.90 to 9.60 Mcd m^{-2} (+22%), while the EQE rises from 22.0% to 29.0% (+32%). Taller lenses provide stronger refractive redirection and improved optical matching at the encapsulant/air interface, thereby mitigating photon trapping associated with waveguiding and total internal reflection and

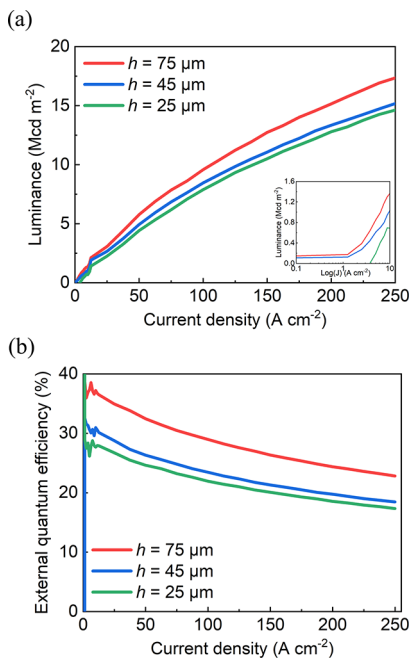


Figure 6. Dependence on microlens morphology (height/aspect ratio): (a) forward luminance and (b) EQE of microlens-encapsulated devices with $h = 25, 45$, and $75 \mu\text{m}$ as a function of current density. Inset in (a): luminance replotted with a logarithmic current-density axis to facilitate comparison in the low-current regime.

enhancing light-extraction efficiency. In our process, the lens height is controlled within $\pm 5\%$ (postcure), ensuring reproducible performance across arrays. In addition to the height control ($\pm 5\%$ after curing), the microlens width (aperture diameter, w) is also well controlled, as confirmed by statistical extraction from a representative $5\times$ FOV ($N = 48$) (Figure S3 and Table S2).

Table 1 summarizes the drive current density J required to reach target luminances of 1, 5, and 10 Mcd m^{-2} . Planar encapsulation demands substantially higher J across all levels ($31/70/194 \text{ A cm}^{-2}$), whereas the microlens-encapsulated device with $h = 75 \mu\text{m}$ requires only $18/43/106 \text{ A cm}^{-2}$, corresponding to -42% , -39% , and -45% relative to planar at $1/5/10 \text{ Mcd m}^{-2}$, respectively. It also outperforms the bare chip ($21/46/112 \text{ A cm}^{-2}$) by -14% , -6.5% , and -5.4% at the same targets. The benefit scales with lens height: $h = 45 \mu\text{m}$ needs $22/51/128 \text{ A cm}^{-2}$ (-34% vs planar at 10 Mcd m^{-2}), and $h = 25 \mu\text{m}$ needs $28/58/139 \text{ A cm}^{-2}$ (-28% vs planar). These results confirm that microlenses lower the required drive current density to reach a given brightness by improving light extraction, which is advantageous for thermally constrained, high-density arrays.

Because the junction temperature rise is strongly tied to electrical power ($I\text{-}V$) under continuous operation, reducing the required current density at a given luminance is expected to mitigate self-heating and improve thermal headroom for dense-array operation in communication/CPO modules.

Figures 7 and 8 compare the angular characteristics using complementary metrics. Figure 7 plots the non-normalized angular illuminance (lx) under a constant current. The planar film suppresses on-axis emission and concentrates the output between $\sim 60^\circ$ and 120° , which is a characteristic signature of photon trapping by total internal reflection and waveguiding within the planar encapsulation layer. In contrast, the

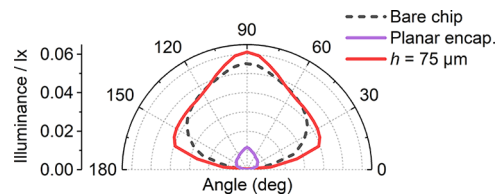


Figure 7. Non-normalized angular illuminance (lx) under constant current for bare, planar, and microlens ($h = 75 \mu\text{m}$) devices, highlighting stronger on-axis emission with microlenses.

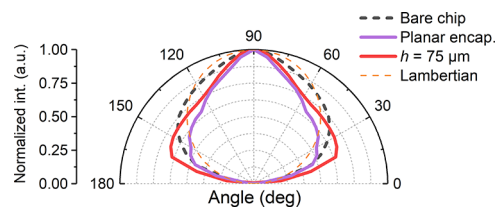


Figure 8. Normalized angular intensity of bare, planar, and microlens devices with a Lambertian reference, showing redistribution toward the surface normal while maintaining wide-angle coverage.

microlens-encapsulated device ($h = 75 \mu\text{m}$) exhibits a substantially broader usable range ($\sim 30^\circ$ – 150°) and a pronounced enhancement at 90° (surface normal). This redistribution originates from refraction at the curved microlens interface, which redirects high-angle components that would otherwise undergo TIR and waveguiding back into the escape cone, thereby reducing waveguiding-related trapping losses and enhancing near-normal emission while maintaining wide-angle coverage.

Figure 8 shows the normalized angular intensity together with a Lambertian reference. After normalization, the microlens sample still presents a stronger near-normal lobe while retaining wide-angle tails, confirming genuine pattern reshaping rather than a mere scaling of absolute output. Depending on lens geometry (e.g., height/curvature), the array can be configured for either narrow-angle, high-directionality coupling or wide-angle coverage. Accordingly, h/w serves as the more general geometric descriptor for LEE and emission directionality, while h is used in the main text as a practical tuning knob under approximately fixed- w conditions. Consistent with this interpretation, the simulations in Figure S2 were performed under a fixed aperture (lens diameter = $150 \mu\text{m}$) while varying only the lens height, thereby isolating the role of curvature (h/w) from aperture-size effects. Additional height-dependent polar plots and the experiment–simulation correlation versus h/w are provided in the Supporting Information (Figures S1 and S2).

Considering all results—structural uniformity, optical output, and angular distribution—our microlens packaging consistently outperforms both planar and unencapsulated cases in terms of luminance, EQE, required drive current density (at specified luminance targets), and emission coverage. Its core strengths are pixel-level alignment precision and customizable geometry, yielding high LEE, controllable directionality, and lower required drive current density. Thus, this microlens encapsulation strategy is promising for high-speed optical communication modules and CPO devices, and offers a scalable fabrication path for multiwavelength (e.g., RGB) microlens arrays and heterogeneous integration.^{25,26}

To extend this lithography-free approach to multiwavelength (e.g., RGB) arrays, the microlens geometry can be codesigned

for each wavelength by incorporating polymer dispersion and the intrinsic emission profiles of the R/G/B subpixels. Practically, color-specific microlens arrays (e.g., different h/w and, if needed, aperture w) can be preformed and fully cured on separate donor stamps, and then sequentially transfer-printed onto the corresponding R/G/B subpixel regions using the same CCD-referenced alignment frame. This modular workflow avoids additional photolithography on the device wafer while enabling wavelength-tailored beam shaping and coupling to free-space/fiber/waveguide optics in VLC and CPO modules.

4. CONCLUSION

We have introduced a mass-transfer-compatible packaging strategy that simultaneously aligns and forms microlenses during chip transfer, achieving array-level registration of $\approx \pm 1\text{ }\mu\text{m}$ while simplifying the process flow. Under 100 A cm^{-2} , the microlens-encapsulated micro-LED reaches 9.6 Mcd m^{-2} and 29% EQE, up from 6.5 Mcd m^{-2} and 19% for planar encapsulation, respectively. The curved lens redistributes the radiation pattern—enhancing near-normal output and widening angular coverage—and lowers the drive current density required to meet specified luminance targets. This lithography-free, scalable route is well suited to VLC, CPO, and related high-speed optoelectronic modules. Future efforts will target RGB lens codesign, improved heterogeneous coupling, and quantitative thermo-mechanical reliability assessments (e.g., thermal cycling, damp-heat storage, and long-term operation) to validate stability under application-relevant conditions. Further engineering toward ultrahigh-resolution microdisplays will require submicron overlay control via higher-resolution vision alignment, closed-loop motion stages, and low-distortion stamp/carrier designs to suppress fractional overlay error and optical crosstalk.

■ ASSOCIATED CONTENT

SI Supporting Information

The Supporting Information is available free of charge at <https://pubs.acs.org/doi/10.1021/acsaom.Sc00641>.

Additional experimental and analytical details including droop-efficiency definition and extracted droop values (Table S1); aperture-width statistics and distribution derived from optical micrographs (Table S2, Figure S3); angular-emission quantification at selected viewing angles and corresponding metrics (Table S3); and supplementary photographs/measurement setups and procedures (Figures S1 and S2) ([PDF](#))

■ AUTHOR INFORMATION

Corresponding Author

Tsung-Hao Su — Department of Materials Science and Engineering, National Tsing Hua University, Hsinchu 300, Taiwan; orcid.org/0009-0008-7272-2586; Email: s107031801@m107.nthu.edu.tw

Authors

Ming-Yu Lou — Department of Materials Science and Engineering, National Tsing Hua University, Hsinchu 300, Taiwan

Wen-De Xie — Department of Materials Science and Engineering, National Tsing Hua University, Hsinchu 300, Taiwan

Ting-Hao Liu — Department of Materials Science and Engineering, National Tsing Hua University, Hsinchu 300, Taiwan

Sun-Zen Chen — Center for Nanotechnology, Materials Science, and Microsystems, National Tsing Hua University, Hsinchu 300, Taiwan

Jwo-Huei Jou — Department of Materials Science and Engineering, National Tsing Hua University, Hsinchu 300, Taiwan; orcid.org/0000-0002-9413-0206

Complete contact information is available at:

<https://pubs.acs.org/10.1021/acsaom.Sc00641>

Notes

The authors declare no competing financial interest.

■ ACKNOWLEDGMENTS

The authors gratefully acknowledge Yu-Chun Lee and Wei-Yuan Ma of Lextar Electronics Corporation for their valuable contributions to this research, and Hsien-Chieh Tsen for expert assistance with figure preparation.

■ REFERENCES

- (1) Di Vito, A.; Amiri, P.; Bornemann, S.; Schöttler, G.; Vergin, M.; Meierhofer, F.; Gülink, J.; Waag, A.; Canals, J.; Diéguez, A.; Prades, J. D.; Auf der Maur, M. Design Study of a Micro Illumination Platform Based on GaN MicroLED Arrays. *Appl. Opt.* **2023**, *62* (28), 7503–7511.
- (2) Wu, T.; Sher, C. W.; Lin, Y.; Lee, C. F.; Liang, S.; Lu, Y.; Huang Chen, S. W.; Guo, W.; Kuo, H. C.; Chen, Z. Mini-LED and Micro-LED: Promising Candidates for the Next Generation Display Technology. *Appl. Sci.* **2018**, *8*, 1557.
- (3) Huang, Y.; Hsiang, E. L.; Deng, M. Y.; Wu, S. T. Mini-LED, Micro-LED and OLED Displays: Present Status and Future Perspectives. *Light Sci. Appl.* **2020**, *9*, 105.
- (4) Liu, X.; Lin, R.; Chen, H.; Zhang, S.; Qian, Z.; Zhou, G.; Chen, X.; Zhou, X.; Zheng, L.; Liu, R.; Tian, P. High-Bandwidth InGaN Self-Powered Detector Arrays toward MIMO Visible Light Communication Based on Micro-LED Arrays. *ACS Photonics* **2019**, *6* (12), 3186–3195.
- (5) Le Maitre, P.; Cibie, A.; Rol, F.; Jacob, S.; Michit, N.; El Badaoui, S.; Simon, J.; Miralles, B.; Ballot, C.; Aventurier, B.; De Martino, P. Short-Range Optical Communication with GaN-on-Si Micro-LED and Micro-PD Matrices. *J. Soc. Inf. Display* **2024**, *32* (12), 797–814.
- (6) Tian, P.; Liu, X.; Yi, S.; Huang, Y.; Zhang, S.; Zhou, X.; Hu, L.; Zheng, L.; Liu, R. High-Speed Underwater Optical Wireless Communication Using a Blue GaN-Based Micro-LED. *Opt. Express* **2017**, *25* (2), 1193–1201.
- (7) Jin, H.; Lin, Z.; Lai, W.; Jiang, H.; Cai, J.; Chen, H.; Hao, W.; Ye, Y.; Xu, S.; Yan, Q.; Guo, T.; Chen, E. Micro-LED Retinal Projection for Augmented Reality Near-Eye Displays. *Laser Photonics Rev.* **2025**, *19*, 2402083.
- (8) Lv, Z.; Liu, X.; Wu, S.; Zhang, W.; Yue, C. P.; Liu, Z. Massive GaN Micro-LED Array Based Underwater Wireless Optical Communication. *Opt. Express* **2025**, *33* (9), 19527–19534.
- (9) Hang, S.; Chuang, C.-M.; Zhang, Y.; Chu, C.; Tian, K.; Zheng, Q.; Wu, T.; Liu, Z.; Zhang, Z.-H.; Li, Q.; Kuo, H.-C. A Review on the Low External Quantum Efficiency and the Remedies for GaN-Based Micro-LEDs. *J. Phys. D: Appl. Phys.* **2021**, *54*, No. 153002.
- (10) Olivier, F.; Tirano, S.; Dupré, L.; Aventurier, B.; Largeron, C.; Templier, F. Influence of Size-Reduction on the Performance of GaN-Based Micro-LEDs for Display Application. *J. Lumin.* **2017**, *191*, 112–116.

- (11) Ding, K.; Avrutin, V.; Izyumskaya, N.; Özgür, Ü.; Morkoç, H. Micro-LEDs, a Manufacturability Perspective. *Appl. Sci.* **2019**, *9* (6), 1206.
- (12) Wierer, J. J.; Tansu, N. III-Nitride Micro-LEDs for Efficient Emissive Displays. *Laser Photonics Rev.* **2019**, *13* (9), 1900141.
- (13) Wu, Y.-E.; Hsu, J.-H.; Chen, K.-H.; Tien, K.-C.; Chen, L.-Y.; Kuo, H.-C. Enhanced Micro-LED Light Efficiency by Optical Structures on Substrate. *J. Soc. Inf. Display* **2025**, *33* (7), 842–851.
- (14) Kumar, V.; Kymmissis, I. MicroLED/LED Electro-Optical Integration Techniques for Non-Display Applications. *Appl. Phys. Rev.* **2023**, *10* (2), No. 021306.
- (15) Choi, H. W.; Liu, C.; Gu, E.; McConnell, G.; Girkin, J. M.; Watson, I. M.; Dawson, M. D. GaN Micro-LED Arrays with Monolithically Integrated Sapphire Microlenses. *Appl. Phys. Lett.* **2004**, *84* (13), 2253–2255.
- (16) Zhu, L.; Lai, P.-T.; Choi, H.-W. LED with Integrated Microlens Array Patterned by an Ultraviolet Linear Micro-LED Array. *Proc. IEEE Photonics Global Conf.* **2010**, 52–54.
- (17) Wang, C.; Fan, Y.; Wang, B.; Yang, H.; Shao, J. Fully Enclosed Composite Micro/Nano-Package for High-Quality Micro-LED Display Pixels and In Situ Nanoimprint Technology. *Adv. Mater. Technol.* **2024**, *9* (6), 2301782.
- (18) Chen, E.; Yao, Z.; Fan, Z.; Lai, W.; Liang, T.; Yan, Q.; Guo, T.; Chen, C. P. Collimated LED Array with Mushroom-cap Encapsulation for Near-eye Display Projection Engine. *IEEE J. Sel. Top. Quantum Electron.* **2024**, *30* (2), 1.
- (19) Chen, E.; Fan, Z.; Zhang, K.; Huang, C.; Xu, S.; Ye, Y.; Sun, J.; Yan, Q.; Guo, T. Broadband Beam Collimation Metasurface for Full-Color Micro-LED Displays. *Opt. Express* **2024**, *32* (6), 10252–10264.
- (20) Ni, Y.; Feng, D.; Ma, D. Design of Freeform Microlens Arrays with Prescribed Luminance Distributions for MicroLED Optical Packaging. *Appl. Opt.* **2025**, *64* (27), 7875–7884.
- (21) Bower, C. A.; Meitl, M. A.; Raymond, B.; Radauscher, E.; Cok, R.; Bonafede, S.; Gomez, D.; Moore, T.; Prevatte, C.; Fisher, B.; Rotzoll, R.; Melnik, G. A.; Fecioru, A.; Trindade, A. J. Emissive Displays with Transfer-Printed Assemblies of $8 \mu\text{m} \times 15 \mu\text{m}$ Inorganic LEDs. *Photonics Res.* **2017**, *5* (A1), A23–A29.
- (22) Corbett, B. M.; Loi, R.; Zhou, W.; Liu, D.; Ma, Z. Transfer Print Techniques for Heterogeneous Integration of Photonic Components. *Prog. Quantum Electron.* **2017**, *52*, 1–17.
- (23) Zhang, Q.; Schambach, M.; Schlisske, S.; Jin, Q.; Mertens, A.; Rainer, C.; Hernandez-Sosa, G.; Heizmann, M.; Lemmer, U. Fabrication of Microlens Arrays with High Quality and High Fill Factor by Inkjet Printing. *Adv. Opt. Mater.* **2022**, *10*, 2200677.
- (24) Zhu, X.; Xu, Q.; Hu, Y.; Li, H.; Wang, F.; Peng, Z.; Lan, H. Flexible Biconvex Microlens Array Fabrication Using Combined Inkjet-Printing and Imprint-Lithography Method. *Opt. Laser Technol.* **2019**, *115*, 118–124.
- (25) Jin, Z.; Yan, L.; Zhu, S.; Cui, X.; Tian, P. 10-Gbps Visible Light Communication in a 10-m Free Space Based on Violet Series-Biased Micro-LED Array and Distance Adaptive Pre-Equalization. *Opt. Lett.* **2023**, *48* (8), 2026–2029.
- (26) Du, Y.; Wang, F.; Hong, Z.; Shi, Y.; Chen, X.; Zheng, X. Detachable Interface toward a Low-Loss Reflow-Compatible Expanded-Beam Edge Coupling for Co-Packaged Optics (CPO). *Opt. Express* **2023**, *31* (2), 1318–1329.



CAS BIOFINDER DISCOVERY PLATFORM™

CAS BIOFINDER HELPS YOU FIND YOUR NEXT BREAKTHROUGH FASTER

Navigate pathways, targets, and diseases with precision

Explore CAS BioFinder

